Hot- and Cold-Case Orbits for Robust Thermal Control

Derek W. Hengeveld,* James E. Braun,† and Eckhard A. Groll‡
Purdue University, West Lafayette, Indiana 47907
and
Andrew D. Williams§
U.S. Air Force Research Laboratory, Kirtland Air Force Base,
New Mexico 87117

DOI: 10.2514/1.44468

Realizing cheaper, more flexible alternatives to traditional satellites requires robust design approaches. Robust satellite subsystems are designed to meet a broad range of mission requirements; consequently, they drastically reduce nonrecurring engineering costs and greatly diminish design, development, assembly, integration, and test schedules. Robust thermal control subsystems must be capable of handling a broad range of thermal environments, thus reducing design and development costs but can be susceptible to overdesign. Therefore, improved design methodologies are needed to maintain their advantages while minimizing excessive design. As a first step, design hot- and cold-case orbits should be examined. The primary goal of the study described in this paper was to identify single hot- and cold-case design orbits that work well in the design of robust thermal control subsystems over a wide range of satellite surface properties and likely operating environments. A general approach was developed to identify worst-case orbits that employ a combination of statistical and historical data such that statistically insignificant orbits are disregarded. Using this method, individual hot- and cold-case design orbits were found at beta angle/ inclination combinations of 72 deg /52 deg and 0 deg /28 deg, respectively. The use of these design orbits works well for a wide range of different satellite surface properties.

Nomenclature

a	=	semimajor axis, km
$c(\theta)$	=	albedo correction term, dimensionless
$\bar{c}$	=	average albedo correction term, dimensionless
$\cos(\theta)$	=	cosine solar zenith angle, dimensionless
D	=	current day, day
d	=	days from J2000.0, days
E''	=	Earth-emitted irradiation, W/m²
F_{s-E}	=	view factor from spherical satellite to spherical Earth, dimensionless
f	=	eclipse fraction, dimensionless
g	=	mean anomaly, deg
h	=	low-Earth-orbit altitude, km
i	=	inclination of orbit, deg
JD	=	Julian Day, day
K	=	orbital-averaged albedo flux correction factor, dimensionless
L	=	mean longitude of the Sun, deg
M	=	current month, month
P	=	orbital period, min
$\bar{q}''$	=	orbital-averaged extreme external environmental heat load, W/m²
$\bar{q}''_{\text{alb}}$	=	orbital-averaged albedo flux, W/m²
$\bar{q}''_{\text{OLR}}$	=	orbital-averaged outgoing longwave radiation flux, W/m²
$\bar{q}''_{\text{sol}}$	=	orbital-averaged direct solar flux, W/m²
R_E	=	Earth's radius, 6378 km
r	=	spherical satellite radius, m
S''	=	direct solar irradiation, W/m²
t	=	time, day
Y	=	current year, year
α	=	surface solar absorptivity, dimensionless
β	=	beta angle, deg
β^*	=	cutoff beta angle used to determine eclipse fraction, deg
γ	=	reference direction in mean equinox of date system
δ	=	declination of the sun, deg
ε	=	obliquity of ecliptic, deg
ε	=	surface longwave emissivity, dimensionless
θ	=	solar zenith angle, deg
λ	=	ecliptic longitude, deg
ν	=	true anomaly, deg
ρ_{alb}	=	albedo fraction, dimensionless
$\bar{\rho}_{\text{alb}}$	=	average albedo, dimensionless
$\rho_{\text{alb}}(0\,\text{deg})$	=	albedo fraction at solar zenith angle of 0 deg, dimensionless
$\rho_{\text{alb}}(\theta)$	=	solar zenith angle dependent albedo, dimensionless
φ	=	angular orbital position measured at zero at the most-nearly subsolar point, deg
Ω	=	right ascension of the ascending node, deg
Ω_o	=	right ascension of the ascending node at initial time, deg
Ω_{sun}	=	right ascension of the sun, deg
Ω_{J_2}	=	orbital variation of right ascension of the ascending node, deg/day

Superscripts/Subscripts

cold	=	cold case
hot	=	hot case

*Research Assistant, School of Mechanical Engineering, Ray W. Herrick Laboratories, 140 S. Martin Jischke Drive. Student Member AIAA.
†Professor, School of Mechanical Engineering, Ray W. Herrick Laboratories, 140 S. Martin Jischke Drive.
‡Professor, School of Mechanical Engineering, Ray W. Herrick Laboratories, 140 S. Martin Jischke Drive.
§Research Scientist, Space Vehicles Directorate, 3550 Aberdeen Avenue SE. Member AIAA.

I. Introduction

ENVIRONMENTAL heating plays a significant role in the design and development of spacecraft thermal control subsystems

Table 1 Review of hot- and cold-case design orbits used for robust thermal control subsystem development

TCS approach	Altitude, km	i, deg	β, deg	S'', W/m^2	ρ_{alb}, dimensionless	Earth-emitted radiation
			Hot-case design orbits			
TherMMS [5]	400.0	60	40	1414	0.28	260.5 K
TherMMS [5]	400.0	0	0	1414	0.26	266.0 K
TherMMS [5]	800.0	Sun synchronous	90	1414	0.27	260.2 K
FACTS [6]	200.0	NA	90	1414	0.57	275.0 W/m^2
SMARTS [7]	185.2	NA	90	1354	0.35	225.0 W/m^2
			Cold-cased design orbits			
TherMMS [5]	400.0	60	40	1322	0.18	248.7 K
TherMMS [5]	400.0	0	0	1322	0.14	251.8 K
TherMMS [5]	800.0	Sun synchronous	90	1322	0.18	249.0 K
FACTS [6]	1000.0	NA	0	1322	0.18	218.0 W/m^2
SMARTS [7]	185.2	NA	0	1354	0.35	225.0 W/m^2

aNA: This information was not available in the cited work.

(TCS). Consequently, orbital parameters, which influence direct solar, albedo, and Earth-emitted heat fluxes, must be carefully evaluated over their expected range. Traditionally, extreme heating environments are identified for a particular mission and hot- and cold-case design orbits are established. However, despite consistent data, there is not a commonly accepted methodology in design orbit development [1]. Approaches include those where TCS design influences mission concepts [2] and others where a given mission dictates specific hot- and cold-case design orbits [3].

Recently, robust spacecraft have gained much attention. Although this approach has significant advantages, it also presents new challenges. Whereas hot- and cold-case design orbits for traditional missions are established from a well-defined spacecraft attitude and orientation, robust TCS bounding orbit conditions must be based on a broad range of potential orbit definitions. Consequently, determining limiting hot and cold cases in a manner appropriate for robust missions is problematic. Further, the range of methodologies and resulting design orbits that have been used is noteworthy. For example, in optimizing the Brazilian Multimission Platform TCS, hot- and cold-case design orbits were established for each of several mission classes (e.g., equatorial and sun synchronous) [4]. Several other robust TCS efforts include thermal management for modular satellites (TherMMS), forced air convection thermal switches (FACTS), and satellite modular and reconfigurable thermal system (SMARTS). Although these approaches are intended for the same broad range of missions, they are based on significantly different hot- and cold-case design orbits (Table 1). Not only does this lead to potentially inconsistent development efforts, but without careful analysis can result in over or underdesigned systems. Therefore, establishment of a uniform set of hot- and cold-case design orbits using a consistent methodology is necessary in the development of robust TCS.

In this paper, the need for robust and, furthermore, responsive satellites is discussed. Ensuing challenges facing the design and development of robust TCS are presented. Of these, determining limiting hot- and cold-case orbits is addressed. To achieve this objective, a general approach was developed to identify worst-case orbits that employs a combination of statistical and historical data such that statistically insignificant orbits are disregarded. Results of

this approach provide unique hot- and cold-case design orbits that bound the design of robust thermal control subsystems over a wide range of satellite surface properties and likely operating environments without being overconstraining or forcing significant overdesign.

II. Robust Spacecraft

Space exploitation provides tremendous opportunities. Since 1957, satellites have been developed to take advantage of this new high-ground by providing communication, scientific observation, weather monitoring, navigation, remote sensing, surveillance, and data-relay services [8]. However, space presents extraordinary challenges. Consequently, satellites have become exceedingly complex and costly. Current satellites can take from 3 to 7 years to deploy (Table 2) and cost from millions to billions of dollars [10].

Increased complexity and cost can be traced to the growing importance and expectations of space. In addition, high launch costs push manufacturers to extend design life to reduce life-cycle costs [11]. However, extended design life is accomplished through added redundancy that in turn increases complexity and cost. Until recently, affordable space exploitation has remained elusive. Although current costs to place a kilogram of capability on orbit remain expensive, modern advances have significantly increased the capability resident in every kilogram, thus opening the door for small satellites (i.e., <500 kg) [12].

Developed in the late 1980s, small satellites have the capability to increase launch rates, increase space-based solutions to common terrestrial problems, and aid in developing a more robust aerospace industry [11]. These advantages are realized through cost savings resulting from decreased mass (both bus and launch vehicle), reduced complexity, limited redundancy, utilization of existing and off-the-shelf technology, and shortened design schedules. In addition, reduced on-orbit lifetimes provide cost savings and have a side effect of making technology insertion much easier than larger programs [13]. Finally, small satellites spread risk. Whereas loss of a large complex system presents a potentially disastrous situation, loss of a small satellite does not because they are easier to replenish.

More flexible and even cheaper satellites can be realized through robust design approaches. Robust satellites are designed to meet a broad range of mission requirements; consequently, they drastically reduce nonrecurring engineering costs and greatly diminish design, development, and assembly, integration, and test schedules (Table 3). This table illustrates advantages of robust design above traditional and small satellite approaches, the primary being reduced development time. Responsive space (RS) is a modern example of robust satellites that challenge the boundaries of schedule limits while keeping costs low.

III. Responsive Space

Current space systems are point designs that have been carefully optimized to meet worst-case conditions for a specific mission. Because of the level of design and development required for systems,

Table 2 Design and development schedule requirements for varying spacecraft complexities [9]

——	Assemble, test, and launch operations, months	Total design and development schedule, months
Low-complexity spacecraft	12	44–45
Medium-complexity spacecraft	15	48–55
High-complexity spacecraft	22	78–83

Table 3 Comparison of traditional, small, and robust satellite design approaches

Design approach	Mission flexibility	System performance	Risk tolerance	Development time	Cost	System focus
Traditional/military	Low	High	Low	High	High	Performance
Traditional/commercial	Low	High	Low	High	High	Profit
Traditional/experimental	Low	High	Mid	Mid	High	Science
Small	Mid	Low	Mid	Mid	Mid	Cost
Robust	High	Mid	Mid	Low	Low[a]	Time

[a]High initial cost for development units with low cost for subsequent (i.e., production) units.

they are expensive and schedule intensive. In addition, the United States is more dependent on space assets than any other nation, especially for military applications such as surveillance, communication, navigation, meteorology, theater support, and force application [10,14]. Although these assets currently provide an asymmetric advantage and have positioned the United States as the clear leader in the use of space, this situation is not guaranteed in the future [12]. To reduce development time and cost while maintaining the United States' military space authority, an RS vision has been initiated. RS is an effort of the United States Department of Defense to revolutionize the methods in which satellites are designed, developed, and put into use.

The objectives of RS include providing space support to tactical theaters in less than six days and keeping mission life-cycle costs low [15,16]. In addition, RS has the potential to provide low-cost, reliable spacecraft and launch vehicles. The Operationally Responsive Space (ORS) office has been directed to strive for satellite costs under $40 million and launch costs under $20 million [17]. RS mission characteristics will fall into one of two categories. First, tailored tactical intelligence, surveillance, communications, and reconnaissance missions will be used to employ imagers and real-time blue force tracking capabilities. Second, space control missions will be used to sense threats against and provide protection for United States space assets [18]. In total, these efforts will potentially increase security of the United States and its allies, increase the use of remote sensing, provide disaster relief, increase monitoring of earthquake activity, and provide a teaching tool for universities [15].

In effect, the goal of RS is to demonstrate operationally responsive, low-cost, 500 kg (or less) satellites and launch capability to support warfighter and intelligence needs [19]. To meet this challenge, the methodologies used to design, manufacture, test, launch, and deploy satellites must radically change. Meeting the objectives of RS will require a shift from custom-built satellites to a modular, robust approach [20]. A modular, robust bus is assembled from modular components with standard interfaces and minimal interdependencies between modules. It is an approach with open-standards and interfaces, self-describing components, and an autoconfiguring system. System integration is simple and testing tasks are automated although in the early developmental states extensive system integration and testing is required. In addition, RS will ultimately use state-of-the-industry as opposed to state-of-the-art technologies to keep costs low [21]. A significant evolution in satellite bus design and development is essential.

Traditional thermal control architectures are not well suited to modular spacecraft and, as a result, a robust TCS capable of operating under a variety of scenarios is imperative [22]. Development of a robust TCS able to meet the challenges of RS will prove to be one of the most significant obstacles. Although it can rely on relaxed design methodologies to align with the philosophy of RS, it must be robust enough to meet a considerably larger design space over traditional optimized systems.

IV. Robust Thermal Control Subsystem Design

Robust TCS should be capable of handling a broad range of mission requirements and thermal environments. If accomplished, both cost and schedules are greatly reduced. One challenge is meeting these goals without excessive overdesign. This presents significant problems due to the relatively large and complex design space. For example, the thermal engineer must account for payload

selection, bus configuration (i.e., component selection and placement), orbit definition, and time-varying parameters (e.g., spacecraft orientation). These challenges are augmented by the fact that insufficient time is available to appropriately design, model, and test in a traditional manner. Whereas traditional thermal control subsystem design methodologies provide highly optimized and capable systems that respond to a specific set of mission requirements, robust TCS must be designed and developed before mission call up. This presents myriad challenges. For example, traditional hot- and cold-case conditions are established from a well-defined spacecraft attitude and orientation [1]. For robust TCS design, bounding orbit conditions provide an immediate hurdle due to the large number of potential orbit definitions. Consequently, determining limiting hot and cold cases in a manner appropriate for robust missions is daunting.
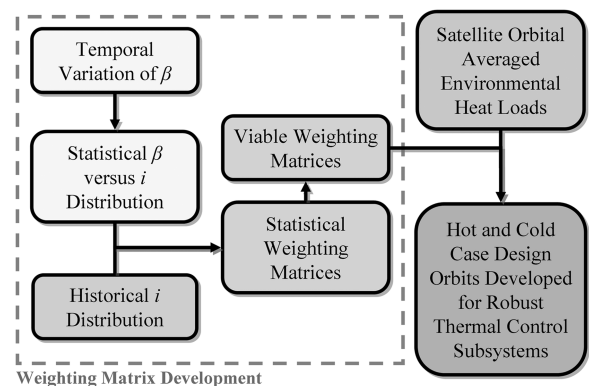
V. Analysis Methodology

The primary goal of the study described in this paper was to identify single hot- and cold-case design orbits that bound the design of robust thermal control subsystems over a wide range of satellite surface properties and likely operating environments without being overconstraining or forcing significant overdesign. To achieve this objective, a general approach was developed to identify worst-case orbits, which employs a combination of statistical and historical data such that statistically insignificant orbits are disregarded (Fig. 1).

First, temporal β relationships were developed based on traditional methods. From this, β versus i relationships were developed, which provided a statistical distribution. These results were combined with historical launch information to generate statistical and subsequently viable weighting matrices. The viable weighting matrices were applied to orbital-averaged thermal environmental models to eliminate statistically insignificant orbits. Using this approach, hot- and cold-case design orbits were found at distinct β and i combinations.

VI. Development of Weighting Matrices

Weighting matrices were developed based on statistical β development and historical i information. These were subsequently applied to orbital-averaged thermal environmental models to eliminate statistically insignificant orbits. This analysis started with a development of the temporal variation of β.

Fig. 1 Overview of analysis methodology.

A. Temporal Variation of β

β is the minimum angle between the solar vector and the orbit plane and can vary from -90 deg to 90 deg where the sign describes the direction of orbit as viewed from the sun. Satellites with positive β appear to be going counterclockwise whereas negative β indicate a clockwise direction. β is a function of both sun coordinates and orbital elements as shown in Eq. (1) [8]

$$\beta = \sin^{-1}[\cos(\delta) \cdot \sin(i) \cdot \sin(\Omega - \Omega_{sun}) + \sin(\delta) \cdot \cos(i)] \quad (1)$$

Several of the parameters that are used to calculate the β change with time. To better understand β, its temporal variation was investigated. The analysis begins by providing a method of describing time in orbit from which sun coordinates and orbital elements are determined.

1. Julian Day (JD)

Calendar time is not convenient for computations, especially over long time intervals. The universally adopted time measure for astronomical problems is the JD, which is a continuous count of the number of days since Greenwich noon on 1 January 4713 B.C. [23]. The following algorithm yields an integer value of JD at noon universal time given a certain Y, M, and D [23,24]

$$JD = D - 32,075 + 1461 \cdot [Y + 4800 + (M - 14)/12]/4$$
$$+ 367 \cdot [M - 2 - (M - 14)/12 \cdot 12]/12 - 3 \cdot \{[Y + 4900$$
$$+ (M - 14)/12]/100\}/4 \quad (2)$$

The current epoch, or standard moment in time upon which orbital elements are referenced, is J2000.0, which is defined as 1 January 2000. Given the current JD, d was found by the following [23]:

$$d = JD - 2451545.0 \quad (3)$$

This value was used to directly determine the β for any given JD.

2. Sun Coordinates

Unless otherwise noted, sun coordinates were based on a low-precision method that provides the equation of time to a precision of $0^m.1$ between 1950 and 2050 due to expansion truncation and coordinates of the sun to 0.01 deg [24,25]. The coordinate system mean equinox of date (MOD) is based on the intersection of the ecliptic and equatorial planes (i.e., γ direction) on a given date [24]. The MOD reference frame accounts for motion of the coordinate system as a result of gravitational forces [25].

The Ω_{sun} is the angular distance measured eastward along Earth's equator from the equinox to a plane perpendicular to the Earth's equator and passing through the sun (i.e., hour circle) [24–26].

$$\Omega_{sun} = \lambda - \left(\frac{180}{\pi}\right) \cdot \tan^2\left(\frac{\varepsilon}{2}\right) \cdot \sin(2 \cdot \lambda)$$
$$+ \left(\frac{180}{2 \cdot \pi}\right) \cdot \left(\tan^2\left(\frac{\varepsilon}{2}\right)\right)^2 \cdot \sin(4 \cdot \lambda) \quad (4)$$

The δ is the angular distance north or south of Earth's equator measured along the hour circle [25]

$$\delta = \sin^{-1}[\sin(\varepsilon) \cdot \sin(\lambda)] \quad (5)$$

The λ is defined as the angular distance measured eastward along the ecliptic (i.e., the mean plane of the Earth's orbit around the sun) from the equinox to a plane passing through the poles of the ecliptic and the celestial object

$$\lambda = L + 1.915 \deg \cdot \sin(g) + 0 \deg .020 \cdot \sin(2 \cdot g) \quad (6)$$

The ε is the angle between the planes of the equator and the ecliptic and varies with JD due to gravitational perturbations [25]

$$\varepsilon = 23.439 \deg - 0 \deg .0000004 \cdot d \quad (7)$$

Mean motion is a measure of the average angular velocity of an object. Therefore, L approximates the ecliptic longitude. The g describes the angle from the perihelion (i.e., the point where Earth is closet to the sun) of an Earth moving with constant angular speed equal to the mean motion. This approximates the ν. These values were determined from the following and subsequently truncated to put them in the range of 0–360 deg [25]

$$L = 280.461 \deg + 0.9856474 \deg \cdot d \quad (8)$$

$$g = 357.529 \deg + 0.9856003 \deg \cdot d \quad (9)$$

3. Orbital Elements

Orbital i will remain constant unless subjected to an external force. These include man-made plane changes and naturally occurring lunisolar forces. Man-made plane changes were not included in this analysis and natural changes have been found to be very small ($\sim 1/100°$ per year) such that the i was assumed constant [27]. For select i (e.g., 0 deg), the right ascension of the ascending node (RAAN) can be assumed constant. For all other i, changes in RAAN due to orbital perturbations are not negligible and must be included.

The equations for sun coordinates presented in the previous section were developed under the following assumptions: 1) gravity is the only force, 2) a spherically symmetric Earth, 3) the Earth's mass is much greater than the satellite's, and 4) the Earth and the satellite are the only two bodies in the system. Gravity is not the only force acting upon a satellite. Additional perturbing forces are present: solar radiation pressure, atmospheric drag, gravitational forces of the sun and moon, and forces as a result of a nonspherical Earth. Of these, perturbations due to a nonspherical Earth dominate the other sources. Therefore, they were the only type of perturbations used in this study [23].

The Earth has a bulge at the equator (oblateness) of approximately 22 km as a result of its rotation [28]. Because of this, periodic variations in the orbital elements are present that are dominated by variations in the RAAN and the argument of perigee. Precession due to Earth's oblateness for circular orbits was approximated by Eq. (10) and is a function of a and i [23]

$$\dot{\Omega}_{J_2} \cong -2.06474 \times 10^{14} \cdot a^{-\frac{7}{2}} \cdot \cos(i) \quad (10)$$

Using the orbit precession and given a RAAN at the beginning of the simulation, a corresponding RAAN at any subsequent time was calculated by Eq. (11)

$$\Omega = \Omega_o + \dot{\Omega}_{J_2} \cdot t \quad (11)$$

Figure 2 shows β variation over a period of one year for i of 0, 30, 60, 90, and 110 deg and an altitude of 1000 km. The initial time and RAAN were 21 March 2007 and 0 deg, respectively.

As shown in Fig. 2, the β varies continuously throughout the year because of orbital perturbations. For example, at an i of 0 or 90 deg, perturbations caused by Earth's oblateness are inconsequential and therefore, the resulting variation of β follows the declination of the sun over a year. At other i, orbital perturbations play an important part in the resulting change of β versus time. For example, at an i of 98 deg and altitude of 650 km, the orbit is sun synchronous.

B. Statistical β Versus i Distribution

For a given i there is a unique probability distribution for the β. Some β may have zero probability at specific i (e.g., i of 0 deg and β of 90 deg). For each integer i angle shown in Fig. 2, temporal β data were recorded every 0.001 days over one year (i.e., 365,000 data points). Each β was rounded to the nearest integer and used to increment 1 deg bins. The resulting frequency of occurrence values were normalized by the peak value (Fig. 3).
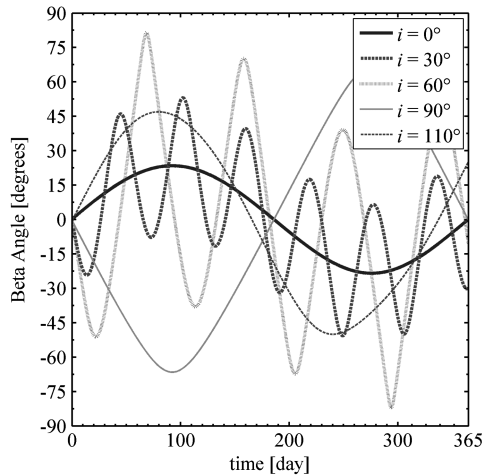
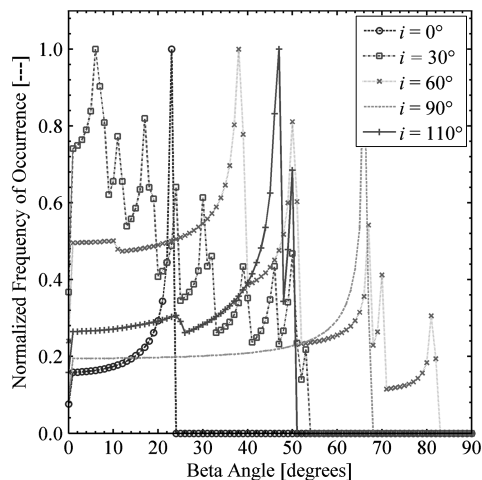Fig. 2 β versus time for select i at an altitude of 1000 km (beginning on 21 March 2007 and RAAN = 0 deg).

Fig. 3 Normalized frequency of occurrence for β for select i at an altitude of 1000 km (beginning on 21 March 2007 and RAAN = 0 deg).

For a given i, a maximum normalized frequency of occurrence is apparent at a particular β. For example, at an i of 60 deg, a maximum occurs at a β of approximately 38 deg. For this particular i, this is the β that occurred most often at an h of 1000 km and a RAAN of 0 deg. The normalized frequency of occurrence becomes zero for combinations of β and i that are not possible.
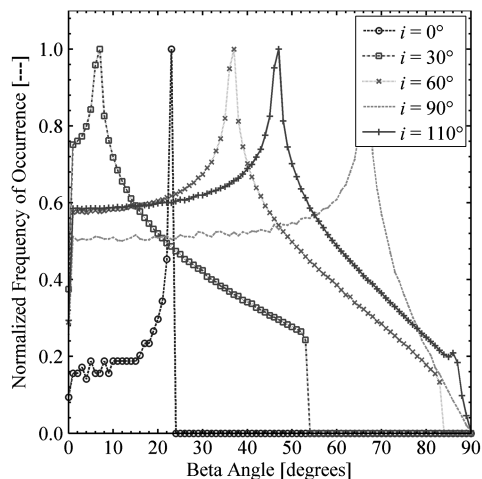

Fig. 4 Normalized frequency of occurrence for β for select i at altitudes of 350–1000 km (beginning on 21 March 2007 and RAAN of 0–360 deg).

Figure 4 provides similar results to those of Fig. 3 but expands the analysis space to include summed results for integer β from 0 to 90 deg, select i from 0 to 110 deg, integer RAANs from 0 to 360 deg, and h from 350 km to 1000 km at a step size of 50 km. Figure 5 shows the same information but as a contour plot for all i from 0 to 110 deg.

Figures 4 and 5 indicate that for a given i, there is a well-defined peak in the normalized frequency of occurrence. Furthermore, there is a range of β where the frequency of occurrence goes to zero. These figures clearly indicate a relationship of maximum normalized frequency of occurrence versus β and i that follows $\approx \pm (i + 23.4)$.

The expected distribution of β as a function of i presented in Fig. 5 can be used to statistically predict the potential of encountering a specific β for a given i. For example, from Fig. 5 at an i of 90 deg, the β most often encountered is approximately 67 deg. It must be noted that this is based on a blended distribution with information obtained from a range of altitudes (350 km to 1000 km) and a range of RAANs (0–360 deg) over a period of one year. In addition to capturing information over a broad range of orbital variables, this approach also had a tendency to smooth the resulting distribution. This can readily be verified by examining Figs. 3 and 4 for select i.

β at a given i can be disregarded if the continuous time spent at that combination is significantly less than typical low-Earth-orbit (LEO) orbital periods of approximately 90 min. This would potentially occur for i with relatively high perturbation frequencies (i.e., the number of oscillations over the course of one year). Investigation showed that these worst-case scenarios still yielded times on the order of hours and therefore all feasible combinations of β and i must be included in the analysis and cannot be disregarded. For example, at an $i = 30$ deg from Fig. 2, which displays relatively high perturbation frequencies, continuous time spent at a given β is no less than approximately 7 h.

C. Historical i Distribution

Historically, satellites in LEO have been launched into a finite number of i regions. For example, i around 63.4 deg will follow a Molniya orbit [23] whereas those between 96.8 and 99.5 deg are sun synchronous. Communication satellites such as the 66 Iridium satellites use near-polar 86.4 deg i and the 48 Globalstar satellites use 52 deg i orbits. Conversely, some i are seldom, if ever, used. To account for variations in application, a probability distribution of i was sought based on historical launch information. Data from 1957 to 2006[¶] were obtained for 29,493 unclassified orbiting objects (i.e., satellites, debris, and rocket fairings). To eliminate debris and rocket fairing information, these data were cross-referenced with satellite launch information.[**] The resulting data set included 949 satellites launched into LEO with perigee greater than 350 km and apogee less than 1000 km. This included circular and elliptic orbits with maximum eccentricity of 0.03. For each object, specific orbital i information was obtained and the frequency of occurrence was tabulated and normalized for integer values of i from 0 to 110 deg. The results are shown in Fig. 6. This figure provides an expected distribution of i based on a historical perspective that can be used to statistically predict the potential of encountering a specific i.

D. Weighting Matrices

The statistical β versus i and historical i distributions were combined into weighting matrices that were subsequently used in the search for hot- and cold-case design orbits. Weighting matrices helped focus the search by eliminating statistically insignificant orbits. A statistical weighting matrix was developed first and was found to eliminate much of the available search space. As a result, this approach was modified to include all viable combinations of β and i at a given threshold level. The result was the development of viable weighting matrices.
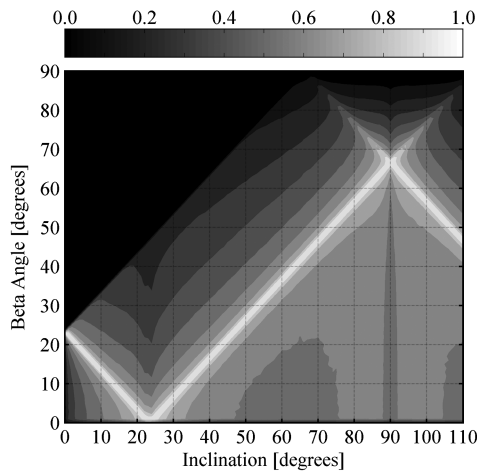
Fig. 5   Contour plot of normalized frequency of occurrence for β for i at altitudes of 350–1000 km (beginning on 21 March 2007 and RAAN of 0–360 deg).
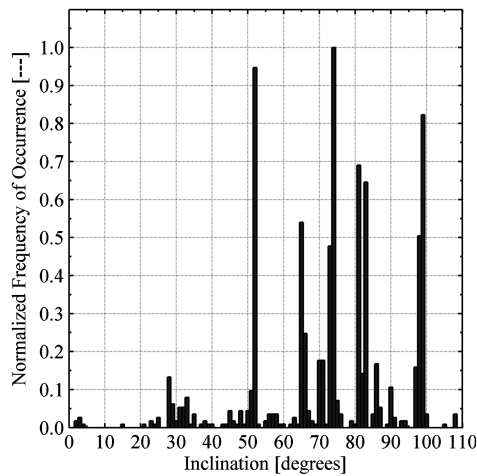

Fig. 7   Contour plot of statistical weighting matrix based on Hadamard product of β vs i distribution and historical i distribution information.

Fig. 6   Historical i distribution based on LEO satellite launches from 1957 to 2006.

Fig. 8   Contour plot of viable weighting matrix for combinations of β and i at a threshold of 0.00.

1.   Statistical Weighting Matrices

The probability that a particular combination of β and i angle will occur can be estimated from the product of the frequency that the β can occur at that particular i angle (Fig. 4) and the probability of occurrence of the i angle based on historical data (Fig. 6). With this in mind, a discrete statistical weighting matrix was developed using data from Figs. 4 and 6 with 1 deg bin sizes for β and i angles. For β from 0 to 90 deg and i from 0 to 110 deg, this resulted in the Hadamard product (term by term) of a 91×111 matrix and a 1×111 matrix. The resulting 91×111 matrix was normalized and plotted as a contour plot as shown in Fig. 7.

As shown in Fig. 7, the majority of β and i combinations were at or near zero. Consequently, resulting design orbits were found to be limited to those β and i combinations with values close to or at 1.0 from Fig. 7 (e.g., $\beta = 50$ deg, $i = 74$ deg). In effect, using the statistical weighting matrix eliminated most of the possible design orbit candidates. As a result, a modified approach was taken to increase the search space without losing the valuable information residing in the statistical weighting matrix. The result was the development of viable weighting matrices.

2.   Viable Weighting Matrices

The statistical weighting matrix includes values from zero (i.e., combinations not possible) up to one. To ensure that all possible combinations of β and i were given consideration, a viable weighting matrix was generated. This weighting matrix was created by
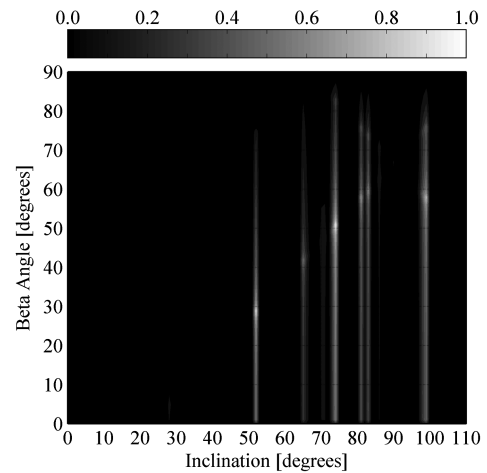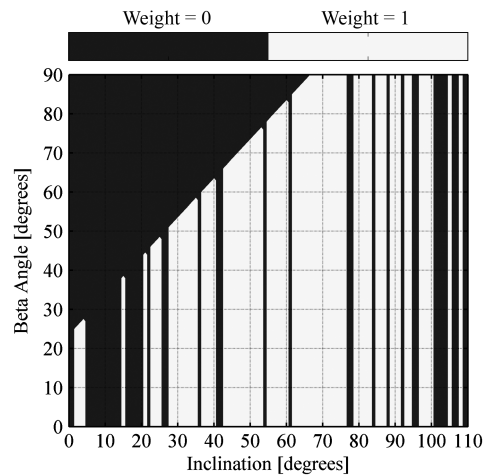
converting all statistical weighting matrix values greater than a given threshold to one. In effect, the viable weighting matrix maximizes the search space at a given threshold. In addition, increasing threshold values reduce the size of the search space. Figures 8 and 9 show viable weighting matrices for thresholds of 0.00 and 0.03; areas in yellow indicate the search space at the given threshold value. Viable
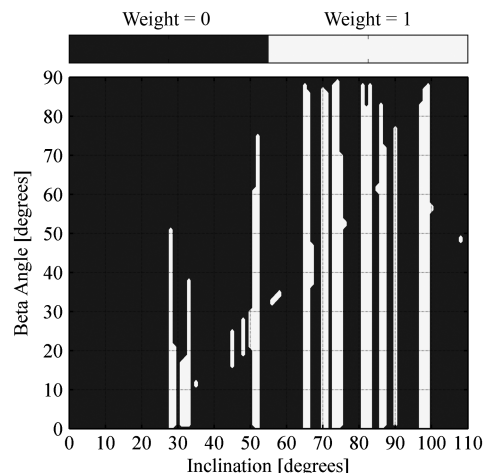

Fig. 9   Contour plot of viable weighting matrix for combinations of β and i at a threshold of 0.03.

weighting matrices at thresholds of 0.01, 0.02, 0.04, 0.05, 0.10, 0.20, 0.25, 0.26, 0.30, and 0.50 were also generated for use in developing hot- and cold-case design orbits.

VII. Satellite Orbital-Averaged Environmental Heat Loads

The next step in determining the design hot- and cold-case orbital parameters was to quantify orbital-averaged maximum hot- and minimum cold-case external environmental heat loads. Four distinct satellite surface types were considered that cover the range of expected solar absorptivity and longwave emissivity properties as summarized in Table 4.

These surface types were applied to a spherical satellite model in circular orbit. The metrics for hot- and cold-case heat loads were orbital-averaged external environment heat flux values consisting of three primary components: direct solar, albedo, and outgoing longwave radiation (OLR) flux (i.e., Earth-emitted radiation).

A. Orbital-Averaged Direct Solar Flux $\bar{q}''_{sol}$

Direct solar flux is a product of irradiation emanating from the sun that arrives uninterrupted on a satellite S'' and surface solar absorptivity α. Accounting for a shape factor of $\frac{1}{4}$ (i.e., $\pi \cdot r^2 / 4 \cdot \pi \cdot r^2$) and eclipse fraction f the orbital-averaged direct solar flux, per unit satellite surface area, can be calculated as shown in Eq. (12)

$$\bar{q}''_{sol} = \alpha \cdot S'' \cdot \frac{1}{4} \cdot (1 - f) \qquad (12)$$

Eclipse occurs for only certain orbits. For example, an orbit with a β of 0 deg will have an eclipse, and the orbit with a β of 90 deg will not. The fraction of time a circular orbit is in eclipse (i.e., eclipse fraction) was calculated using Eq. (13) [1]

$$f = \frac{1}{180} \cdot \cos^{-1} \cdot \left[\frac{(h^2 + 2 \cdot R_E \cdot h)^{\frac{1}{2}}}{(R_E + h) \cdot \cos(\beta)} \right] \quad \text{if } |\beta| < \beta^*$$
$$f = 0 \quad \text{if } |\beta| \geq \beta^* \qquad (13)$$

where

$$\beta^* = \sin^{-1} \left[\frac{R_E}{(R_E + h)} \right] \quad \text{for } 0 \deg \leq \beta^* \leq 90 \deg \qquad (14)$$

The spectral shape of solar irradiation S'' is approximated by a blackbody at 5777 K and as a result is primarily shortwave radiation. For an Earth-orbiting spacecraft, the magnitude of this value is not constant. First, the sun emitted energy varies with an 11-year solar cycle although this effect is only a fraction of a percent [29]. This phenomenon follows the mean sunspot number [30]. Second, because the Earth's orbit is elliptical, the mean distance between the Earth and sun varies approximately ±1.7% throughout the year. As a result, direct solar flux varies ±3.4% [29]. Accounting for an additional ±5 W/m² due to variations in the solar cycle, solar irradiation values range from 1317 W/m² (S''_{cold}) up to 1419 W/m² (S''_{hot}) depending upon the Earth's position relative to the sun.

B. Orbital-Averaged Albedo Flux $\bar{q}''_{alb}$

Albedo flux is defined as the amount of direct solar flux upon a planet that has been reflected back into space and lands upon a satellite's surface in combination with surface optical properties.

Table 4 Surface properties for the four surface categories

Surface category	Description	α	ε
Flat absorber	Black Z306 polyurethane paint (3 mil thick)	0.95	0.87
Flat reflector	Polished aluminum	0.15	0.05
Solar absorber	Black chrome on nickel foil	0.90	0.10
Solar reflector	Optical solar reflector (diffuse)	0.10	0.80

Because albedo flux emanates from solar irradiance, its spectral shape is similar to the sun's spectrum and, therefore, is primarily composed of shortwave radiation. As a result, surface solar absorptivity becomes important. Assuming Earth is a diffusely reflecting sphere and accounting for altitude effects, the satellite's view of Earth and solar zenith angle θ orbital-averaged albedo flux takes the form shown in Eq. (15)

$$\bar{q}''_{alb} = \alpha \cdot S'' \cdot F_{s-E} \cdot \bar{\rho}_{alb} \cdot K \qquad (15)$$

Assuming the satellite is much smaller than Earth, the view factor from a spherical satellite to a spherical Earth is given by Eq. (16)

$$F_{s-E} = \frac{1}{2} \cdot \left[1 - \frac{(h^2 + 2 \cdot h \cdot R_E)^{1/2}}{R_E + h} \right] \qquad (16)$$

Albedo, ρ_{alb}, is defined as the fraction of incident solar energy reflected or scattered by a planet back into space and as a result, its value ranges from zero to one [29]. A value of zero indicates a planet surface that is highly absorptive to shortwave radiation, whereas a value of one indicates a planet surface that is highly reflective. Albedo values vary significantly depending upon the composition and properties of the planet and atmospheric surfaces. Refer to [31,32] for a detailed investigation of these relationships.

Albedo varies at different locations on Earth and as a result is a function of several variables, including local Earth and atmospheric conditions (which are correlated to latitude) and solar zenith angle. These values, based upon the Earth radiation budget experiment (ERBE), are summarized in several sources [1,32]. Average albedo $\bar{\rho}_{alb}$ is obtained by averaging the solar zenith angle-dependent albedo $\rho_{alb}(\theta)$ over noneclipse portions of orbital period P. When in eclipse, the value of $\rho_{alb}(\theta)$ becomes zero. Accounting for the effects of solar zenith angle, Eq. (17) results [32]

$$\bar{\rho}_{alb} = \frac{\int_0^P \rho_{alb}(\theta) \cdot S'' \cdot \cos(\theta) \cdot dt}{\int_0^P S'' \cdot \cos(\theta) \cdot dt}$$
$$= \frac{\int_0^P (\rho_{alb}[(0 \deg) + c(\theta)] \cdot S'' \cdot \cos(\theta) \cdot dt}{\int_0^P S'' \cdot \cos(\theta) \cdot dt} \qquad (17)$$

which can be rewritten as

$$\bar{\rho}_{alb} = \rho_{alb}(0 \deg) + \bar{c} \qquad (18)$$

Albedo values at a solar zenith angle of 0 deg $\rho_{alb}(0 \deg)$ were collected from the ERBE, which includes data as a function of three distinct i bands (i.e., 0–30, 30–60, and 60–110 deg) for several averaging periods (i.e., 16, 128, and 896 s, 30 and 90 min, and 6 and 24 h). The 16-s time averaging data provide the most extreme values. For the analysis, 90-min time-averaged values were chosen, which were the closest to the period of LEO orbits.

To reduce the size and corresponding complexity of available data, three extreme combinations were identified: albedo, combined, and OLR [30]. Albedo extreme values consist of a pair of albedo and OLR values for which 0.04% of the values exceed the given albedo value. Combined extreme values occur when 0.04% of the values are both above and to the right of the value for the hot-case extreme and 0.04% of the values are both below and to the left of the value for the cold-case extreme. OLR extreme values occur when 0.04% of the values exceed the given OLR value. These three are illustrated in Fig. 10. For each of these extremes, mission critical values based on 3.3σ values in which the values are exceeded 0.04% of the time were used.

The average correction term $\bar{c}$ was determined by Eq. (19)

$$\bar{c} = \frac{\int_0^P c(\theta) \cdot \cos(\theta) \cdot dt}{\int_0^P \cos(\theta) \cdot dt} \qquad (19)$$

Equation (19) can be simplified by relating the values of θ, β, and φ (which defines the angular position around the orbit measured at zero at the most-nearly subsolar point) using Eq. (20) [32]
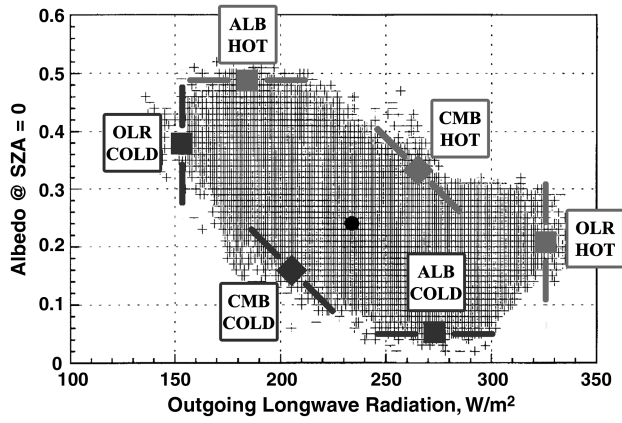
Fig. 10 Albedo vs OLR for medium *i* orbits (30–60°) using 128 s data averaging [30].

$$\cos(\theta) = \cos(\beta) \cdot \cos(\varphi) \qquad (20)$$

For a circular orbit, φ varies linearly with time and thus, integration was made with respect to angular position. Noting that the value of $c(\theta)$ becomes invalid in eclipse and substituting Eq. (20) into Eq. (19) yields Eq. (21):

$$\bar{c} = \frac{\int_0^P c(\theta) \cdot \cos(\beta) \cdot \cos(\varphi) \cdot dt}{\int_0^P \cos(\beta) \cdot \cos(\varphi) \cdot dt} = \frac{\int_{-\frac{\pi}{2}}^{\frac{\pi}{2}} c(\theta) \cdot \cos(\varphi) \cdot d\varphi}{\int_{-\frac{\pi}{2}}^{\frac{\pi}{2}} \cos(\varphi) \cdot d\varphi}$$

$$= \frac{1}{2} \cdot \int_{-\frac{\pi}{2}}^{\frac{\pi}{2}} c(\theta) \cdot \cos(\varphi) \cdot d\varphi \qquad (21)$$

The average correction term was solved numerically and results are given as a function of β in Table 5 [32].

Assuming Earth is a diffusely reflecting sphere, incident albedo flux is a function of eclipse, a satellite's view of Earth (sunlit versus shaded portions), and $\cos(\theta)$, among others. For a more rigorous discussion, refer to [33]. On an orbital-averaged basis, these compounding effects were approximated by developing a correction factor K as a function of β. Monte Carlo raytracing software was used to solve Eq. (15) for K over a range of β (0–90 deg) and altitudes (350–1000 km) for unit absorptivity, direct solar flux, and orbital-averaged albedo flux. The results are plotted in Fig. 11.

A resulting cubic regression model fitted to these data revealed the correction factor in Eq. (22) with a coefficient of determination R^2 of 99.8%. As shown, this model fits the data well with modest variance at large β. Because of $\cos(\theta)$ dependence, orbital-averaged albedo flux diminishes as β increases; therefore, these deviations do not significantly impact overall environmental fluxes

$$K = 0.3132 + 0.7678E - 3 \cdot \beta - 0.8034E - 4 \cdot \beta^2$$
$$+ 0.4130E - 6 \cdot \beta^3 \qquad (22)$$

Table 5 Average correction term $\bar{c}$ vs β

β	$\bar{c}$
0	0.04
10	0.04
20	0.05
30	0.06
40	0.07
50	0.09
60	0.12
70	0.16
80	0.22
90	0.31

C. Orbital-Averaged Outgoing Longwave Radiation Flux $\bar{q}''_{OLR}$

Earth maintains an average effective temperature of $-18°C$ and as a result, constantly emits longwave (i.e., infrared) radiation [8]. In addition, the atmosphere is emitting radiation and absorbing Earth-emitted energy. Because of this, the spectral distribution of Earth's emitted radiation is relatively complex. However, it is accepted practice to model this source as a graybody spectrum according to a temperature range of 250–300 K [29]. This yields wavelengths longer than 3 μm [32]. As a result, the orbital-averaged OLR flux is a result of diffuse irradiation emanating from Earth E'' that arrives on a satellite in combination with surface longwave emissivity ε

$$\bar{q}''_{OLR} = \varepsilon \cdot F_{s-E} \cdot E'' \qquad (23)$$

Although OLR flux is less than direct solar flux, it poses a unique problem because the source temperatures are very close to that of the spacecraft. As a result, it cannot be easily reflected away by selecting surface materials with appropriate optical properties because these same types of surfaces would not allow emittance of spacecraft heat.

The orbital-averaged heat flux model for both the hot and cold cases is a combination of the three sources

$$\bar{q}''_{hot} = \bar{q}''_{sol,hot} + \bar{q}''_{alb,hot} + \bar{q}''_{OLR,hot} \qquad (24)$$

$$\bar{q}''_{cold} = \bar{q}''_{sol,cold} + \bar{q}''_{alb,cold} + \bar{q}''_{OLR,cold} \qquad (25)$$

Substituting the three sources provides Eqs. (26) and (27) for the hot and cold cases, respectively [32]

$$\bar{q}''_{hot} = \alpha \cdot S''_{hot} \cdot \left[\frac{1}{4} \cdot (1-f) + F_{s-E} \cdot \bar{\rho}_{alb} \cdot K \right] + \varepsilon \cdot F_{s-E} \cdot E''_{hot} \quad (26)$$

$$\bar{q}''_{cold} = \alpha \cdot S''_{cold} \cdot \left[\frac{1}{4} \cdot (1-f) + F_{s-E} \cdot \bar{\rho}_{alb} \cdot K \right] + \varepsilon \cdot F_{s-E} \cdot E''_{cold} \quad (27)$$

As these equations illustrate, the orbital-averaged hot- and cold-case extreme external environmental heat loads are a function of h, β, i, $\rho_{alb}(0 \text{ deg})$, E'', and surface properties (α and ε). Hot- and cold-case heat fluxes were identified for each surface type and combination of β and i by exhaustively searching over all other applicable variables and finding the extreme (both maximum and minimum) values of Eqs. (26) and (27). The resulting values from this analysis are shown in Figs. 12 and 13 for the flat absorber hot and cold cases, respectively.

Hot-case orbital-averaged extreme heat flux increases with increasing β until a local maximum is reached and then decreases.
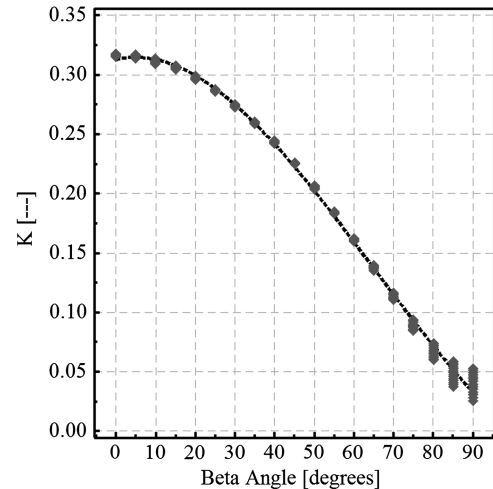

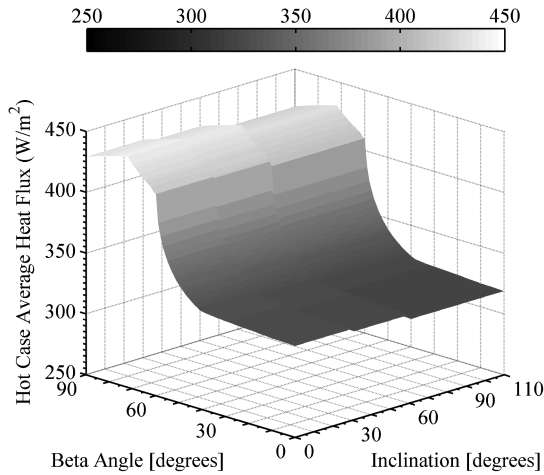**Fig. 11 Orbital-averaged albedo flux correction factor K vs β.**

Fig. 12   Hot-case orbital-averaged extreme heat flux (W/m²) vs β and i (flat absorber).
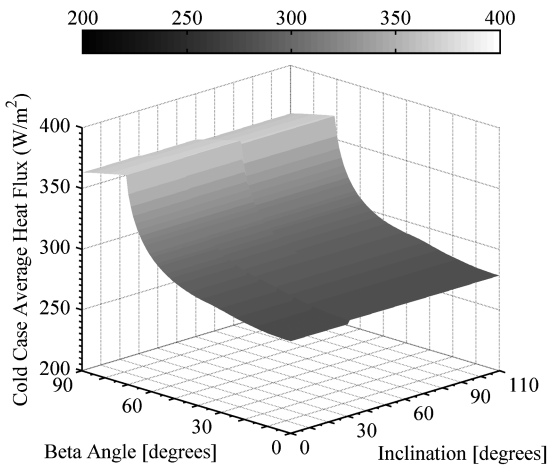

Fig. 13   Cold-case orbital-averaged extreme heat flux (W/m²) vs β and i (flat absorber).

This is a direct result of orbital eclipse fractions. As the β increases, eclipse fractions decrease, which increases the orbital-averaged direct solar and albedo fluxes. A maximum heat flux is reached at the point where eclipse fractions reach zero. As β continues to increase, albedo fluxes diminish.

Because of the nature of albedo and OLR values that came out of the ERBE study, three distinct bands of values appear in the hot-case orbital-averaged extreme heat flux figures. For a given β, the heat flux generally decreases with increasing i. This is the result of eclipse fractions that cause albedo fluxes to be seen over a portion of an orbit,

whereas OLR fluxes are seen over an entire orbit. As a result, OLR fluxes typically dominate albedo fluxes in the orbital-averaged model. For large β and thus, small eclipse fractions, this trend is still prevalent because the orbit is near the terminator where albedo fluxes drop off due to $\cos(\theta)$ dependence. Cold-case orbital-averaged extreme heat flux figures show similar trends to that of the hot-case results. The only difference is the relative magnitude of fluxes that were found. The orbital-averaged hot- and cold-case extreme external environmental heat load results provide insight into design orbits although they do not take into account the probabilities of occurrence for different combinations of β and i. The next section addresses this issue.

VIII.   Hot- and Cold-Case Design Orbits Developed for Robust Thermal Control Subsystems

The viable weighting matrix was applied to the orbital-averaged heat load results. The use of the viable weighting approach provides a method of examining a subset of hot- and cold-case heat flux information without altering their values. The statistical weighting approach tends to smooth the heat flux information. Critical hot- and cold-case orbital parameters were identified by first applying the viable weighting matrix at a 0.00 threshold to the orbital-averaged heat flux models for each of the four surface types. In essence, this method stripped away values that were either not possible (e.g., combinations of β and i) or not statistically significant (e.g., i that historically have not been used). The resulting hot- and cold-case results are shown in Table 6.

For each hot- and cold-case critical orbit and surface type, a single β was found in combination with a set of i that gave the same orbital-averaged heat flux. However, the goal was to define a single pair of β and i for each surface type or possibly for all surface types. As a next step, the threshold was increased for each surface type and hot- and cold-case designs until the set of i was narrowed to one value. Table 7 provides resulting critical hot- and cold-case orbits for each of the four surface categories. As a result of applying increasing threshold values, the set of i have been reduced to one for the same critical hot- and cold-case heat fluxes from Table 6. As shown in Table 7, the threshold level needed was very low (0.03) in all cases except for the cold-case solar reflector. These results were verified within 3.2% of values obtained from Monte Carlo raytracing software.

The results show that critical cold-case orbits occur at β of 0 deg in all cases. This is not surprising because the largest eclipse fractions occur here. Critical hot-case orbits occur at β of 72 deg because this is the angle at which eclipse fraction initially becomes zero at an altitude of 350 km.

The altitudes at which critical cold-case orbits were found show interesting characteristics. Intuitively, it is expected that critical cold-case orbits would occur at high altitudes (i.e., 1000 km). This occurs for the flat absorber and solar reflector cold cases because these have relatively high OLR fluxes, which occur irrespective of eclipse fraction. Thus, high altitudes produce lower fluxes due to view factor

Table 6   Critical weighted orbital-averaged hot- and cold-case orbits for each of four surface categories at a 0.00 threshold

Surface type	α	ε	Heat flux, W/m²	β, deg	i, deg	Earth IR and albedo values[a]	Altitude, km
					Flat absorber		
Hot case	0.95	0.87	437.4	72	49–53, 55–60	3	350
Cold case	0.95	0.87	275.7	0	2–4, 15, 21, 23–25, 28–30	2	1000
					Flat reflector		
Hot case	0.15	0.05	60.9	72	49–53, 55–60	2	350
Cold case	0.15	0.05	37.3	0	2–4, 15, 21, 23–25, 28–30	1	350
					Solar absorber		
Hot case	0.90	0.10	348.5	72	49–53, 55–60	1	350
Cold case	0.90	0.10	206.5	0	2–4, 15, 21, 23–25, 28–30	1	350
					Solar reflector		
Hot case	0.10	0.80	112.2	72	49–53, 55–60	3	350
Cold case	0.10	0.80	63.5	0	62–76, 79–83, 85–87, 89–91, 93, 94, 97–100, 105, 108	3	1000

[a]Value correspondence (1 = ALB, 2 = CMB, 3 = OLR) where ALB represents albedo extreme values and CMB represents combined extreme values [8,32]

Table 7   Critical weighted orbital-averaged hot- and cold-case orbits for each of four surface categories

Surface type	α	ε	Heat flux, W/m^2	Threshold value	β, deg	i, deg	Earth IR and albedo values[a]	Altitude, km
			Flat absorber					
Hot case	0.95	0.87	437.4	0.03	72	52	3	350
Cold case	0.95	0.87	275.7	0.03	0	28	2	1,000
			Flat reflector					
Hot case	0.15	0.05	60.9	0.03	72	52	2	350
Cold case	0.15	0.05	37.3	0.03	0	28	1	350
			Solar absorber					
Hot case	0.90	0.10	348.5	0.03	72	52	1	350
Cold case	0.90	0.10	206.5	0.03	0	28	1	350
			Solar reflector					
Hot case	0.10	0.80	112.2	0.03	72	52	3	350
Cold case	0.10	0.80	63.5	0.26	0	74	3	1,000

[a]Value correspondence (1 = ALB, 2 = CMB, 3 = OLR) [8,32]

Table 8   Hot-case design orbits percent difference analysis (using orbital-averaged values and viable weighting matrices)

β, deg	72	%	72	%	72	%	72	%
i, deg	52	Diff.	52	Diff.	52	Diff.	52	Diff.
Earth IR and albedo values[a]	3	——	2	——	1	——	3	——
Altitude, km	350	——	350	——	350	——	350	——
Flat absorber ($\alpha = 0.95/\varepsilon = 0.87$)	437.4	0.0%	434.3	0.7%	421.0	3.7%	437.4	0.0%
Flat reflector ($\alpha = 0.15/\varepsilon = 0.05$)	60.9	0.0%	60.9	0.0%	60.4	0.9%	60.9	0.0%
Solar absorber ($\alpha = 0.90/\varepsilon = 0.10$)	346.7	0.5%	348.0	0.1%	348.5	0.0%	346.7	0.5%
Solar reflector ($\alpha = 0.10/\varepsilon = 0.80$)	112.2	0.0%	107.8	4.0%	93.6	16.6%	112.2	0.0%
Average	——	0.1%	——	1.2%	——	5.3%	——	0.1%

[a]Value correspondence (1 = ALB, 2 = CMB, 3 = OLR) [8,32]

considerations. For the other two surface types (flat reflector and solar absorber), critical cold-case orbits occur at altitudes of 350 km. This result is caused by the fact that each of these surfaces is driven by albedo fluxes (i.e., solar absorptivity significantly greater than longwave emissivity). As a result, critical cold-case environments occur when eclipse fractions are the greatest. This occurs at the lowest altitudes.

To consider the possibility of defining hot- and cold-case orbiting parameters that work well for any surface type, the design orbit parameters determined for each surface type in Table 4 were applied to the remaining three surface types. For example, the design hot-case orbit for a flat absorber occurred at $\beta = 72$ deg, $i = 52$ deg, Earth infrared (IR) and albedo value = 3, and an altitude of 350 km. At this combination of orbit parameters, the design hot-case heat flux was determined to be 437.4 W/m^2. These same orbit parameters were applied to the flat reflector, solar absorber, and solar reflector surface types. The resulting hot-case heat fluxes were determined and compared with the design hot-case heat fluxes. Results for the hot-case design orbits are shown in Table 8. The percent differences in heat fluxes are in comparison to design values for each surface type and set of orbiting parameters. Average percent differences across the surface types are also given for each unique set of orbit parameters.

As shown in Table 8, the average percent error in heat flux by using a single set of hot-case design orbit parameters ($\beta = 72$ deg,

$i = 52$ deg, Earth IR and albedo values = 3, altitude = 350 km) is minimal (0.1%). In addition, this single hot-case design orbit provided orbital-averaged heat fluxes within 0.5% of the values determined using design orbits specific to individual surface types. It appears that this combination of orbit parameters could be used as a single design point for all surface types including satellites having combined surface properties.

A similar analysis was completed for the cold-case design orbits. As shown in Table 9, the orbit parameters with the lowest average percent heat flux error corresponds to $\beta = 0$ deg and $i = 28$ deg with Earth IR and albedo value = 2 and an altitude of 1000 km. At this design point, the average percent error in heat flux by using a single set of cold-case design orbit parameters is −4.7%. Although still small, this value is notably influenced by the solar reflector results (i.e., percent difference of −9.0%). It could be argued that a separate design cold-case orbit ($\beta = 0$ deg, $i = 74$ deg, Earth IR and albedo values = 3, altitude = 1000 km) should be used for spacecraft with predominantly solar reflector surfaces. If this approach is used then a design cold-case orbit ($\beta = 0$ deg, $i = 28$ deg, Earth IR and albedo values = 1, altitude = 350 km) should be used for all other surface types with a maximum percent difference of −3.4%.

Further analysis indicated that hot- and cold-case design orbits also work well for intermediate surface types. An analysis was conducted for a surface with $\alpha = 0.50$ and $\varepsilon = 0.50$. The resulting

Table 9   Cold-case design orbits percent difference (using orbital-averaged values and viable weighting matrices)

β, deg	0	%	0	%	0	%	0	%
i, deg	28	Diff.	28	Diff.	28	Diff.	74	Diff.
Earth IR and albedo values[a]	2	——	1	——	1	——	3	——
Altitude, km	1000	——	350	——	350	——	1000	——
Flat absorber ($\alpha = 0.95/\varepsilon = 0.87$)	275.7	0.0%	285.2	−3.4%	285.2	−3.4%	279.8	−1.5%
Flat reflector ($\alpha = 0.15/\varepsilon = 0.05$)	38.6	−3.3%	37.3	0.0%	37.3	0.0%	40.0	−7.1%
Solar absorber ($\alpha = 0.90/\varepsilon = 0.10$)	220.1	−6.6%	206.5	0.0%	206.5	0.0%	230.3	−11.6%
Solar reflector ($\alpha = 0.10/\varepsilon = 0.80$)	69.2	−9.0%	92.3	−45.5%	92.3	−45.5%	63.5	0.0%
Average	——	−4.7%	——	−12.2%	——	−12.2%	——	−5.0%

[a]Value correspondence (1 = ALB, 2 = CMB, 3 = OLR) [8,32]

critical hot-case orbit was identical to the design point found previously ($\beta = 72$ deg, $i = 52$ deg, Earth IR and albedo values $= 3$, altitude $= 350$ km). The critical cold-case orbit was identical to the design point identified for all surface types ($\beta = 0°$, $i = 28°$, Earth IR and albedo value $= 2$, altitude $= 1000$ km).

IX. Conclusions

Single hot- and cold-case design orbits that work well in the design of robust thermal control subsystems over a wide range of satellite surface properties and likely operating environments were determined. A general approach was developed that employed a combination of statistical and historical data such that statistically insignificant orbits were disregarded. From the analysis, a hot-case design orbit was found ($\beta = 72$ deg, $i = 52$ deg, altitude $= 350$ km) that provided orbital-averaged heat fluxes within 0.5% of the values determined using design orbits specific to individual surface types. A general cold-case design orbit was found ($\beta = 0$ deg, $i = 28$ deg, altitude $= 1000$ km) that provided orbital-averaged heat fluxes within 9.0% of the values determined using design orbits specific to individual surface types. If more accuracy is required, two cold-case design orbits were identified. For spacecraft with predominantly solar reflector surfaces, a cold-case design orbit ($\beta = 0$ deg, $i = 74$ deg, altitude $= 1000$ km) provides minimum orbital-averaged heat fluxes. For all other surface types, a cold-case design orbit was found ($\beta = 0$ deg, $i = 28$ deg, altitude $= 350$ km) that provided orbital-averaged heat fluxes within 3.4% of the values determined using design orbits specific to individual surface types.

These results were based on a spherical satellite model and therefore, care should be taken when significant departures from this assumption are challenged. This includes both geometric and attitude deviations such as those for a sun-pointing solar panel. In addition, the design orbits are intended for LEO missions with altitudes in the range of 350–1000 km. Consequently, their use for highly elliptic orbits and those with relatively large altitudes is not recommended.

The hot- and cold-case design orbits have many potential applications. First, they provide consistent design criteria for the development and comparison of robust thermal control subsystem approaches. In the absence of clearly defined mission criteria, these design orbits also provide a reasonable surrogate. Finally, they are useful for the design of robust spacecraft over a wide range of both satellite surface properties and LEO operating environments.

References

[1] Karam, R., "Satellite Temperature and Thermal Energy Management," *Satellite Thermal Control for Systems Engineers*, Vol. 181, AIAA, Reston, VA, 1998, pp. 1–12.

[2] Diaz-Aguado, M., Greenbaum, J., Fowler, W., and Lightsey, E., "Small Satellite Thermal Design, Test, and Analysis," *Proceedings of SPIE: Modeling, Simulation, and Verification of Space-based Systems III*, Vol. 6221, The International Society for Optical Engineering, Orlando, FL, 2006, pp. 622109-1–622109-12.
doi: 10.1117/12.666177

[3] Megahed, A., and El-Dib, A., "Thermal Design and Analysis for Battery Module for a Remote Sensing Satellite," *Journal of Spacecraft and Rockets*, Vol. 44, No. 4, 2007, pp. 920–926.
doi:10.2514/1.19355

[4] Muraoka, I., Galski, R., de Sousa, F., and Ramos, F., "Stochastic Spacecraft Thermal Design Optimization with Low Computational Cost," *Journal of Spacecraft and Rockets*, Vol. 43, No. 6, 2006, pp. 1248–1257.
doi:10.2514/1.20066

[5] Young, Q., "Thermal Management for Modular Satellites (TherMMS): Final Rept.," Air Force Research Laboratory: Space Vehicles Directorate, AFRL-RV-PS-TR-2008-1073, Kirtland Air Force Base, NM, June 2008.

[6] Williams, A., "Robust Satellite Thermal Control Using Forced Air Convection Thermal Switches for Operationally Responsive Space Missions," Master's Thesis, Univ. of Colorado, Dept. of Aerospace Engineering Sciences, Nov. 2005.

[7] Bugby, D., Zimbeck, W., and Kroliczek, E., "Modular Two-Phase Heat Transfer Based Architecture for Future Responsive Spacecraft," *49th AIAA/ASME/ASCE/AHS/ASC Structures, Structural Dynamics, and Materials Conference*, AIAA Paper 2008-1957, Schaumburg, IL, 2008, pp. 1–12.

[8] Gilmore, D. G., "Spacecraft Thermal Environments," *Spacecraft Thermal Control Handbook: Volume 1: Fundamental Technologies*, 2nd ed., Aerospace Press, El Segundo, CA, 2002, pp. 21–70.

[9] Saleh, J., and Dubos, G., "Responsive Space: Concept Analysis, Critical Review, and Theoretical Framework," *AIAA SPACE 2007 Conference & Exposition*, AIAA Paper 2007-6015, Long Beach, CA, 2007, pp. 1–20.

[10] Williams, A., and Palo, S., "Issues and Implications of the Thermal Control System on Responsive Space Missions," *20th Annual AIAA/USU Conference on Small Satellites*, SSC06-3-1, Utah State Univ., Logan, UT, 2006, pp. 1–12.

[11] Noel, J., Excorpizo, R., and Jones, E., "Transforming the National Spacelift Architecture," *AIAA 2nd Responsive Space Conference*, AIAA Paper RS2-2004-2003, Los Angeles, CA, 2004, pp. 1–8.

[12] Cebrowski, A., and Raymond, J., "Operationally Responsive Space: A New Defense Business Model," *Parameters*, U.S. Army War College Quarterly, Carlisle, PA, Summer 2005, pp. 67–77.

[13] Bearden, D., "Small-Satellite Costs," *Crosslink: The Aerospace Corporation*, Vol. 2, No. 1, Winter 2000–2001, pp. 33–44.

[14] Rumsfeld, D. H., Rept. of the Commission to Assess U.S. National Security Space Management and Organization," U.S. Government Printing Office, Washington, D. C., Jan. 2001.

[15] Wegner, P. M., Hardy, D. A., Hite, D. R., and duBro, G., "Development of Responsive Space Systems at the, U.S. Air Force Research Laboratory, Space Vehicles Directorate," *2nd International Conference on Recent Advances in Space Technologies*, IEEE Publications, Piscataway, NJ, 2005, pp. 109–112.

[16] Arritt, B., Kumar, A., Buckley, S., Hannum, R., Welsh, J., Beard, S., Xinlin, Q., and Wegner, P., "Responsive Satellites and the Need for Structural Health Monitoring," *Proceedings of SPIE: Nondestructive Characterization for Composite Materials, Aerospace Engineering, Civil Infrastructure and Homeland Security*, Vol. 6531, International Society for Optical Engineering, San Diego, CA, 2007, pp. 653109-1–653109-10.
doi: 10.1117/12.714424

[17] Arritt, B., Buckley, S., Ganley, J., Welsh, J., Henderson, B., Lyall, E., Williams, A., Prebble, J., DiPalma, J., Mehle, G., and Roopnarine, "Development of a Satellite Structural Architecture for Operationally Responsive Space," *Proceedings of SPIE: Industrial and Commercial Applications of Smart Structures Technologies*, Vol. 6930, International Society for Optical Engineering, San Diego, CA, 2008, pp. 693001-1–693001-9.
doi: 10.1117/12.776319

[18] Summers, J., "Plug and Play Testbed to Enable Responsive Space Missions," *2005 IEEE Aerospace Conference*, IEEE Publications, Piscataway, NJ, 2005, pp. 557–563.

[19] Wegner, P., and Kiziah, R., "Pulling the Pieces Together at AFRL," *AIAA 4th Responsive Space Conference*, AIAA Paper RS4-2006-4002, Los Angeles, CA, 2006, pp. 1–9.

[20] Lawlor, M., "TacSat Delay Ignites Frustration," *SIGNAL Magazine*, Armed Forces Communications and Electronics Association, Fairfax, VA, July 2006, pp. 37–41.

[21] Raymond, J., Glaros, G., Stadter, P., Reed, C., Finnegan, E., Hurley, M., Merk, C., Kawecki, T., Garner, C., and Jaffe, P., "A TacSat Update and the ORS/JWS Standardized Bus," *AIAA 3rd Responsive Space Conference*, AIAA Paper RS3-2005-1006, Los Angeles, CA, 2005, pp. 1–16.

[22] Young, Q., Stucker, B., Gillespie, T., and Williams, A., "Modular Thermal Control Architecture for Modular Spacecraft," *49th AIAA/ASME/ASCE/AHS/ASC Structures, Structural Dynamics, and Materials Conference*, AIAA Paper 2008–1959, Schaumburg, IL, 2008, pp. 1–8.

[23] Wertz, J. R., and Larson, W. J., "Universal Time and Julian Dates," *Space Mission Analysis and Design*, 3rd ed., Space Technology Library, Microcosm Press, El Segundo, CA, 2005, pp. 913–918.

[24] Vallado, D. A., "Equations of Motion," *Fundamentals of Astrodynamics and Applications*, 3rd ed., Space Technology Library, Microcosm Press, El Segundo, CA, 2007, pp. 1–48.

[25] "The Astronomical Almanac for the Year 2007," *Nautical Almanac Office United States Naval Observatory*, U.S. Government Printing Office, Washington, D.C., 2007.

[26] Wiesel, W., "The Two-Body Problem," *Spaceflight Dynamics*, 2nd ed., McGraw-Hill, New York, 1997, pp. 44–72.

[27] Gopinath, N., Ravindrababu, T., Rao, S., Daniel, D., and Goel, P., "Taking Advantage of Inclination Variation in Resonant Remote-Sensing Satellite Orbits," *Acta Astronautica*, Vol. 55, No. 3-9, 2004,

pp. 453–459.
doi:10.1016/j.actaastro.2004.06.001

[28] Sellers, J. J., "Describing Orbits," *Understanding Space: An Introduction to Astronautics*, 3rd ed., McGraw–Hill, New York, 2005, pp. 153–190.

[29] Anderson, B. J., Justus, C. G., and Batts, G. W., "Guidelines for the Selection of Near-Earth Thermal Environment Parameters for Spacecraft Design," NASA TM-2001-211221, Oct. 2001.

[30] Anderson, B. J., and Smith, R. E., "Natural Orbital Environment Guidelines for Use in Aerospace Vehicle Development," NASA TM-4527, June 1994.

[31] "NASA Space Vehicle Design Criteria (Environment): Earth Albedo and Emitted Radiation," NASA SP-8067, July 1971.

[32] Justus, C. G., Batts, G. W., Anderson, B. J., and James, B. F., "Simple Thermal Environment Model (STEM) User's Guide," NASA TM-2001-211222, Oct. 2001.

[33] Cunningham, F., "Earth Reflected Solar Radiation Input to Spherical Satellites," NASA, Technical Note D-1099, pp. 1–10.

T. Lin
Associate Editor